Fifth International Symposium on Marine Propulsors
SMP'17, Espoo, Finland, June 2017

A Hybrid Numerical Method for Investigating Underwater Sound Propagation of Cavitating Propellers

Ulf Göttsche, Martin Scharf, Stephan Berger, Moustafa Abdel-Maksoud

Institute for Fluid Dynamics and Ship Theory, Hamburg University of Technology, Hamburg, Germany

ABSTRACT

The present article deals with the prediction of the underwater noise induced by ship propellers under consideration of sheet cavitation on the propeller blades. The calculation method is a hybrid approach combining a boundary element calculation method with the Ffowcs-Williams Hawkings equation. The method is applied to different simulation cases with increasing complexity. The final case considers the noise propagation in full-scale for a cavitating propeller in combination with a part of a ship stern. This simulation result is compared to a full-scale measurement.

Keywords

Boundary element method, propeller noise, sheet cavitation, Ffowcs-Wiliams Hawkings, FWH

1 INTRODUCTION

Reducing propeller noise has become increasingly important in the last years. Noise issues are not only related to military vessel application, but merchant ship operators are also facing this problem due to upcoming international regulations. In reality, propeller cavitation occurs in many operation conditions of merchant ships, therefore cavitation issues must be considered in the sound prediction. Additionally, the highest degree of environmental impact takes place in the far field, which increases the need to use a larger simulation domain. Thus, it is highly desirable to provide efficient and robust simulation tools able to predict propeller noise in an accurate manner.

A direct simulation of the hydroacoustic field is a very complex and expensive task. In this work, an alternative and well established approach based on acoustic analogies is used (Ianniello et al., 2014a,b; Bensow and Liefvendahl, 2016). The main idea is to split the complex problem into two much simpler problems: in a first step, the hydrodynamic flow field around the considered body is calculated by conventional flow simulation methods where the compressibility of the flow is neglected – here, the in-house panel code *pan*MARE (Berger et al., 2013) is applied. Then, in a subsequent step, the radiated noise due to the hydrodynamic loads and the displacement of the considered body is approximated by the Ffowcs-Williams Hawkings Equation (FWH-Equation). In the present work, the formulation 1A introduced by Farassat and Brentner (1998) is used in order to calculate the hydroacoustic pressure in the far field taking into account the compressibility of the fluid.

Cavitation is considered as the most important contributor to propeller noise and effort has been made to enhance the tool with respect to the consideration of sheet cavitation. Additionally, a model has been implemented to capture multiple sound wave reflections at the free water surface and at the ground.

The capabilities of the simulation tool are demonstrated by means of an extensive numerical study with increasing complexity. For validation purposes, the case of a pulsating sphere – a simple model of a pulsating cavity – is analysed. This is followed by a propeller case in undisturbed inflow. Finally, a propeller and hull configuration is investigated under cavitating and non-cavitating conditions. These results are compared to a full-scale measurement.

2 HYBRID SIMULATION METHOD

The simulation is split into two calculations.

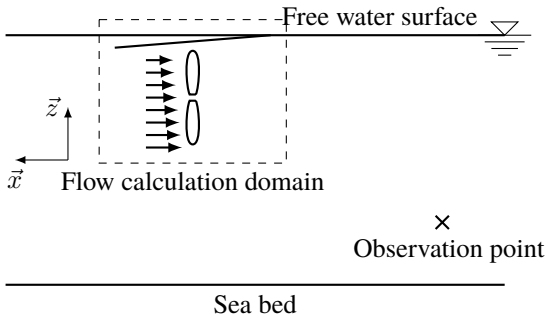

Figure 1: Hybrid BEM and FWH method.

First, the calculation of the flow field is performed (see Figure 1). For every calculation time step, all relevant information for the sound prediction is stored.

After completing the flow calculation, the sound pressure is calculated for the points of interest in the fluid using the stored flow field values. This is a post-processing step, which can be repeated for arbitrary points because the flow calculation is not influenced by the points of interest.

2.1 Flow Calculation Method

The calculation of the fluid domain is performed by the in-house boundary element method *pan*MARE (Berger et al., 2013).

2.1.1 Governing Equations

The flow is assumed to be irrotational, incompressible and inviscid. With this assumption, the governing equations are simplified to the Laplace equation for the velocity potential Φ and the Bernoulli equation for the pressure p (Katz and Plotkin, 2001):

$$\Delta\Phi = \nabla^2\Phi = 0 \tag{1}$$

and

$$p + \rho g z + \frac{1}{2}\rho\left(\nabla\Phi\right)^2 + \frac{\partial\Phi}{\partial t} = \text{const.} \tag{2}$$

The velocity potential is the sum of the potential Φ_{move} due to the movement of the body relative to the earth-fixed coordinate system, the influence of the perturbation potential Φ_{ind} of the body and an arbitrary background flow Φ_{ext}:

$$\Phi = \Phi_{\text{ind}} + \Phi_{\text{ext}} - \Phi_{\text{move}}. \tag{3}$$

A solution for Equation (1) is the Green identity:

$$\Phi_{\text{ind}} = \frac{1}{4\pi}\int_S \left[\frac{1}{r}\nabla\left(\Phi - \Phi_I\right) - \left(\Phi - \Phi_I\right)\nabla\frac{1}{r}\right]\cdot\vec{n}\mathrm{d}S. \tag{4}$$

Here, Φ_I describes the velocity potential inside the body boundaries S and Φ the potential in the flow field. This equation is defined on the boundary S of the fluid domain, which consists of the body boundaries S_B and, considering lifting bodies, the wake S_W. In the equation, a source strength $\sigma = \frac{\partial\Phi_I}{\partial n} - \frac{\partial\Phi}{\partial n}$ and dipole strength $\mu = \Phi_I - \Phi$ is substituted:

$$\Phi_{\text{ind}} = \frac{1}{4\pi}\int_{S_B+S_W}\left[\mu\frac{\partial}{\partial n}\frac{1}{r} - \sigma\frac{1}{r}\right]\mathrm{d}S. \tag{5}$$

The unique solution of the problem is obtained by using the impermeability boundary condition on the body surface S_B. For lifting bodies, the Kutta boundary condition is used at the trailing edge, see Berger et al. (2013) for additional details.

2.1.2 Numerical Implementation

The boundary value problem is solved numerically using a low-order panel method. For this purpose, the boundary of the fluid domain is discretised by quadrilateral panels with constant source and dipole strength on each panel. Equation (5) and the boundary conditions mentioned above yields a system of linear equations which can be solved by the Gauss method (Katz and Plotkin, 2001). Once the velocity distribution is known, the Bernoulli equation delivers the pressure on all body panels.

2.1.3 Sheet Cavitation

Effects of sheet cavitation are modelled by an approach based on the works of Fine (1992) and Vaz (2005). On the cavity surface $S_{B_C} \subset S_B$ additional boundary conditions are postulated. The pressure equals the vapour pressure p_v, which leads to a Dirichlet-like formulation for the potential. Furthermore, no fluid is allowed to penetrate the cavity sheet. The boundary S_{B_C} is unknown and needs to be determined in an iterative manner.

2.2 Sound Prediction Method

2.2.1 Theoretical Model

For the sound prediction, the Ffowcs-Williams Hawkings equation is employed. In this work the integral formulation 1A of Farassat is used (Brentner and Farassat, 2003). This equation is a rearrangement of the Navier-Stokes equation and the continuity equation in the form of an inhomogeneous wave. It can also be interpreted as a generalized form of the Lighthill acoustic analogy. This formulation uses the flow calculation results to determine the acoustic solution:

$$\begin{aligned} p'_T\left(\vec{x}, t^*\right) = &\frac{1}{4\pi}\int_S\left[\frac{\rho_0\left(\dot{v}_n + v_{\dot{n}}\right)}{r\left(1-M_r\right)^2}\right]_{\text{ret}}\mathrm{d}S \\ &+ \frac{1}{4\pi}\int_S\left[\frac{\rho_0 v_n\left(r\dot{M}_r + cM_r - cM^2\right)}{r^2\left(1-M_r\right)^3}\right]_{\text{ret}}\mathrm{d}S \end{aligned} \tag{6}$$

$$\begin{aligned} p'_L\left(\vec{x}, t^*\right) = &\frac{1}{c}\int_S\left[\frac{\dot{l}_r}{r\left(1-M_r\right)^2}\right]_{\text{ret}}\mathrm{d}S \\ &+ \int_S\left[\frac{l_r - l_M}{r^2\left(1-M_r\right)^2}\right]_{\text{ret}}\mathrm{d}S \\ &+ \frac{1}{c}\int_S\left[\frac{l_r\left(r\dot{M}_r + cM_r - cM^2\right)}{r^2\left(1-M_r\right)^3}\right]_{\text{ret}}\mathrm{d}S \end{aligned} \tag{7}$$

$$p'\left(\vec{x}, t^*\right) = p'_T\left(\vec{x}, t^*\right) + p'_L\left(\vec{x}, t^*\right), \tag{8}$$

using the fluid density ρ_0, the body velocity $\vec{v}$ relative to the undisturbed fluid, the distance vector $\vec{r}$ as distance from the sound source point $\vec{y}$ to the observer point $\vec{x}$ with the norm $r = \|\vec{r}\|$, the Mach number $\vec{M} = \frac{\vec{v}}{c}$, the body surface S, the sound speed c and the pressure force $\vec{l} = p\vec{n}$ as pressure p on the body to the fluid in surface unit normal direction $\vec{n}$. A dot over a variable marks a time derivative of that variable. The subscripts n, $\dot{n}$, r and M imply a dot product of that vector variable and the unit normal vector $\vec{n}$ of the surface into the fluid, the time derivative of the unit normal vector $\dot{\vec{n}}$, the unit radiation vector $\hat{\vec{r}}$ or the surface velocity vector $\vec{v}$ normalized by the sound speed c respectively. All values are taken from the source at a retarded time t_{ret} with respect to the sound speed that the information reaches the observer at time t^*. The term p_T (see Equation (6)) describes the influence of the body thickness, while p_L (see Equation (7)) describes the influence of the lifting forces. Terms with r^{-1} dependency are far-field terms, while terms with r^{-2} dependency are near-field terms.

The quadrupole term, which takes into account the contribution of the turbulence, is neglected, as the applied flow calculation method is not able to capture such information.

2.2.2 Implementation

The calculation of the pressure at a point $\vec{x}$ for a time t^* is done for a discretised body surface S. Being a force-free surface, the wake surface S_W does not contribute to radiated pressure per definition. The discretisation is realized by m qualiteral panels (see Section 2.1). The integral values in the Equations (6) and (7) are calculated by a summation over the panel pressure parts. The geometry, motion and pressure of each panel in each time step is known. The values are assumed to be constant over each panel. The time derivative of the pressure is approximated by a second-order interpolation over the previous and next time step. Equations (6) and (7) are transformed to Equations (9) and (10). The variable values are calculated corresponding to Brentner and Farassat (2003):

$$p'_{T,i}\left(\vec{x},t^*\right) = \left(\frac{\rho_0 \left(\dot{v}_n + v_{\dot{n}}\right)}{r\left(1-M_r\right)^2} + \frac{\rho_0 v_n \left(r\dot{M}_r + c\left(M_r - M^2\right)\right)}{r^2 \left|1-M_r\right|^3} \right) \frac{S}{4\pi}\Bigg|_i \quad (9)$$

$$p'_{L,i}\left(\vec{x},t^*\right) = \left(\frac{1}{c}\frac{\dot{l}_r}{r\left(1-M_r\right)^2} + \frac{l_r - l_M}{r^2\left(1-M_r\right)^2} + \frac{1}{c}\frac{l_r \left(r\dot{M}_r + c\left(M_r - M^2\right)\right)}{r^2\left|1-M_r\right|^3} \right) \frac{S}{4\pi}\Bigg|_i \quad (10)$$

$$p'_i\left(\vec{x},t^*\right) = p'_{T,i}\left(\vec{x},t^*\right) + p'_{L,i}\left(\vec{x},t^*\right) \quad (11)$$

$$p'\left(\vec{x},t^*\right) = \sum_{i=1}^{m} p'_i\left(\vec{x},t^*\right). \quad (12)$$

With respect to the sound speed c, the panel values must be taken at emission time $t_{\text{ret}} = t^* - \frac{\|\vec{x}(t^*) - \vec{y}(t)\|}{c}$. Mostly this retarded time t_{ret} is an intermediate time between two calculation time steps $t_1 \leq t_{\text{ret}} \leq t_2$ (see Figure 2), where the body can move between. To reduce the number of interpolations, the FWH pressure parts $p'_i\left(\vec{x}\left(t^*\right), t_1 + \frac{r_1}{c}\right)$ and $p'_i\left(\vec{x}\left(t^*\right), t_2 + \frac{r_2}{c}\right)$ are calculated at the two time steps and then a linear interpolation returns the final pressure part $p'_i\left(\vec{x}\left(t^*\right), t^*\right)$.

2.2.3 Reflection

The equations in Sections 2.2.1 and 2.2.2 describe the direct sound propagation. If the fluid domain is limited by the free surface or walls, which are not modelled by panels, sound reflection needs to be taken into account. The pressure values resulting from different sound paths are calculated separately and then summed up to one result value. To simplify the calculation, reflection surfaces are assumed to be planes.

In general, a reflected pressure can be calculated by mirroring the source at the reflection plane and calculating the additional pressure contribution due to the new source. Because of the different acoustic properties of the materials on both sides of the mirror plane, the additional pressure p'_Γ must be corrected by a reflection factor R (Mei, 2004):

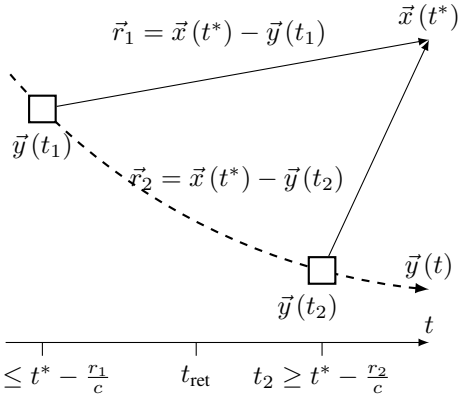

Figure 2: Ffowcs-Williams Hawkings equation interpolation.

$$R = \frac{m\cos^2\Theta - n\sqrt{1 - \frac{\sin^2\Theta}{n^2}}}{m\cos^2\Theta + n\sqrt{1 - \frac{\sin^2\Theta}{n^2}}} \quad (13)$$

$$p'_{\text{sum}}\left(\vec{x},t^*\right) = p'\left(\vec{x},t^*\right) + R p'_\Gamma\left(\vec{x},t^*\right) \quad (14)$$

where $m = \frac{\rho_1}{\rho}$ and $n = \frac{c}{c_1}$. The material properties are represented by the sound speed c and c_1 and the density ρ and ρ_1 of the fluid and the material beyond the reflection plane. The incident angle is named Θ.

Equation (13) returns a real value as result for the free water surface reflection and is used there.

For the reflection on solids more dense than the fluid, Equation (13) returns an imaginary value as result and cannot be used. Instead, a material specific value is taken from measurements or literature. A value of 1 is used in this work, which equals to full reflection.

2.2.4 Cavitation

If cavitation on the body surface exists, the emitting surface for the FWH pressure calculation is changed. The calculation of the pressure uses the body surface increased by the cavity thickness in surface normal direction. The motion of the surface is superset with the change of the cavity thickness in surface normal direction. The pressure force on the surface can be used directly because the flow calculation already returns the vapour pressure.

2.2.5 Time to Frequency Domain Conversion

The method described so far operates in the time domain. Resulting values are converted to the frequency domain by a fast Fourier transform (FFT). To optimize the results, a sample of integer multiples of the most significant period is taken from the time domain. Additionally, a Hanning window is used. The resulting pressure amplitudes in the frequency domain in $[\text{Pa}]$ can be converted to $[\text{dB}]$.

3 NUMERICAL STUDIES

3.1 Pulsating Sphere

To validate the calculation tool, the first calculation case is a pulsating sphere. Sound emission and reflection are validated by means of this example.

The sphere pulsates in an infinite fluid domain. The geometry is shown in Figure 3. In order to evaluate reflection processes, a free water surface and a sea bed have been added. These boundaries are not considered in the fluid simulation.

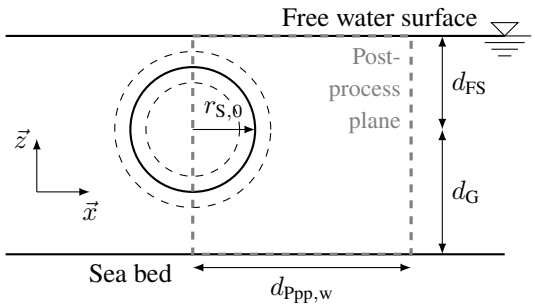

Figure 3: Sphere geometry.

The sphere has an initial radius $r_{\mathrm{S},0}$ and is pulsating with the amplitude Δr_{S} and period T_{S}:

$$r_{\mathrm{S}}(t) = r_{\mathrm{S},0} + \Delta r_{\mathrm{S}} \sin\left(\frac{2\pi}{T_{\mathrm{S}}} t\right). \tag{15}$$

The simulation parameters are listed in Table 1.

Table 1: Sphere calculation parameters.

Characteristics			**Value**
Geometry			
Initial radius	$r_{\mathrm{S},0}$	[m]	0.5
Radius amplitude	Δr_{S}	[m]	0.1
Sphere center relative to free surface	d_{FS}	[m]	10.0
Sphere center relative to sea bed	d_{G}	[m]	90.0
Evaluation plane width	$d_{\mathrm{Ppp,w}}$	[m]	100.0
Simulation			
Period	T_{S}	[s]	0.01
FWH			
Fluid density	ρ_0	$[\mathrm{kg\,m^{-3}}]$	1025.0
Air density	ρ_1	$[\mathrm{kg\,m^{-3}}]$	1.293
Sound speed	c	$[\mathrm{m\,s^{-1}}]$	1500.0
Ground reflection factor	R_G		1.0

After the fluid simulation, the FWH-equation is evaluated on a post-process plane (the gray dashed box in Figure 3) for three different sub cases.

1. Infinite fluid domain.
2. Fluid domain with free water surface.
3. Fluid domain with free water surface and sea bed.

The resulting normalized pressure amplitudes $\hat{p}^*$ of the first order are shown in Figures 4, 5 and 6. The pressure amplitudes $\hat{p}$ are normalized as follows:

$$\hat{p}^* = \frac{\hat{p}}{\rho \left(\frac{\Delta r_{\mathrm{S}}}{T_{\mathrm{S}}}\right)^2}. \tag{16}$$

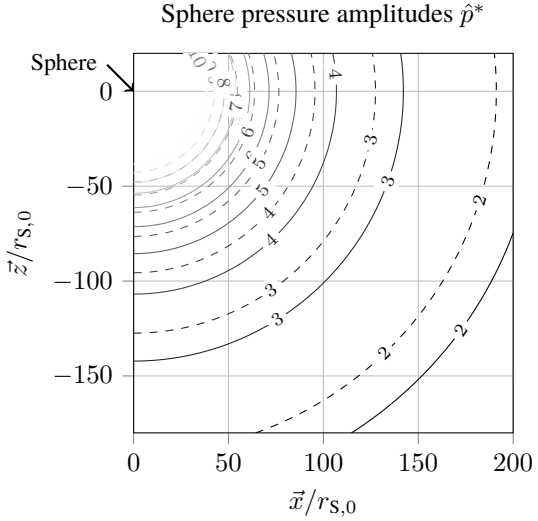

Figure 4: Normalized pressure amplitudes $\hat{p}^*$ (first order) of the pulsating sphere without reflections. FWH: solid; incompressible Bernoulli: dashed.

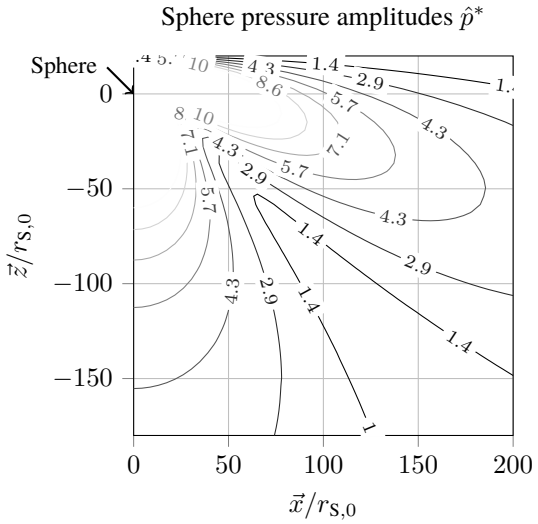

Figure 5: Normalized pressure amplitudes $\hat{p}^*$ (first order) of the pulsating sphere with reflection at the free surface.

The pressure amplitude distribution in Figure 4 compares the distribution of the FWH pressure amplitudes with the incompressible Bernoulli pressure amplitudes of the fluid calculation. Since the FWH-equation takes into account fluid compressibility while the Bernoulli equation assumes an incompressible fluid, the differences between both calculations increases with the distance between source and observer. The pressure amplitudes decrease with the square of the distance for both formulations.

Figure 5 shows the second case featuring an additional free water surface. The superposition of the free surface re-

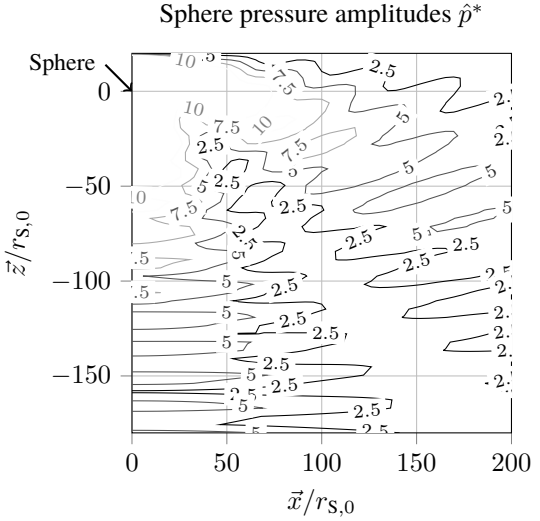

Figure 6: Normalized pressure amplitudes $\hat{p}^*$ (first order) of the pulsating sphere with reflections at the free surface and the sea bed.

flection results in zones of reduced and reinforced pressure amplitudes.

A similar interference pattern is also visible in Figure 6, which presents results from the case with free surface and sea bed reflections. The additional pressure from the sea bed reflection deforms the contours. The free surface reflection amplitudes are larger than the sea bed reflections, so the reduction and reinforcement zones are similar to Figure 5.

The calculated results corresponds to the expected values for this simple application case.

3.2 Propeller

In this section, the noise propagation of a five bladed full-scale propeller in parallel inflow will be investigated. The fluid domain and the sound prediction domain are both unbounded. Each propeller blade is modelled by 22 panels in spanwise and chord direction for pressure as well as suction side. The propeller wake is generated for two revolutions. The relevant simulation settings are listed in Table 2.

The normalized pressure amplitudes $\hat{p}^*$ of the blade frequency are shown in Figure 7. The position and diameter of the propeller is indicated by a small, two-bladed propeller sketch in the diagram. The figure shows the pressure side of the propeller. From the reader's point of view, the rotation direction is clockwise. The pressure amplitudes are normalized as follows:

$$\hat{p}^* = \frac{\hat{p}}{\rho\,(nD)^2}. \tag{17}$$

Figure 8 shows the pressure amplitudes $\hat{p}^*$ of the blade frequency over the dashed line from the propeller to the lower left corner in Figure 7. The value d describes the distance of the observer point to the propeller axis. For comparison, the incompressible Bernoulli pressure is shown in Figure 8. The results are nearly the same as in the comparison for the sphere (see Figure 4).

Table 2: Propeller calculation parameters.

Characteristics			**Value**
Propeller			
Propeller diameter	$D = 2R$	$[\mathrm{m}]$	7.75
Pitch ratio at $r/R = 0.7$	$P_{0.7}/D$		0.977
Area ratio	A_e/A_0		0.732
Hub ratio	d_h/D		0.17
Number of blades	z_P		5
Rotation rate	n	$[\mathrm{s}^{-1}]$	1.25
Thrust loading condition	c_{Th}		0.602
Angle per timestep		$[^\circ\mathrm{s}^{-1}]$	3.00
Fluid			
Fluid density	ρ_0	$[\mathrm{kg\,m}^{-3}]$	1025.0
Air density	ρ_1	$[\mathrm{kg\,m}^{-3}]$	1.293
Sound speed	c	$[\mathrm{m\,s}^{-1}]$	1500.0

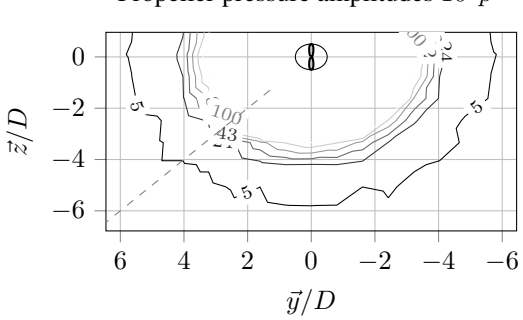

Figure 7: Normalized pressure amplitudes $10^8\hat{p}^*$ (first order) of the propeller.

The diagrams for the higher-order blade frequencies are not shown because their amplitudes are nearly zero.

Figure 7 illustrates the concentric emission of sound, comparable with the sphere results in Figure 4. At the outer radii, the contour plots for the emitted sound amplitudes lose their concentric shape. The diagram in Figure 8 reflects this behaviour. The cause of non-smooth shape is the inaccuracy introduced by the interpolation between two time steps (compare Section 2.2.2). That occurs when the source information for Equations (9) and (10) of different body parts are interpolated using different time step pairs. In this case, the continuous integration over the body surface is not possible. This error scales with the time step size. In addition, the absolute error values are small compared to the pressure amplitudes of a such application case (see Figure 15) and the introduced error is thus negligible.

3.3 Propeller and Hull

The third application case is a simplified full-scale calculation of a stern hull with a propeller. The approximated ship is a 3500 TEU container vessel. The full-scale measurement results are provided by Mecklenburger Metallguss

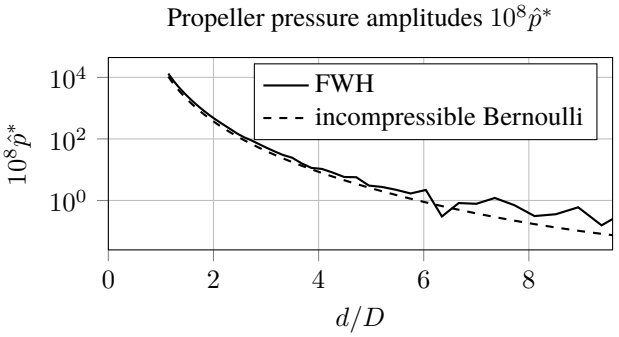

Figure 8: Normalized pressure amplitudes $10^8\hat{p}^*$ (first order) of the propeller over line.

GmbH, further information of the full-scale measurement can be found in (Kleinsorge et al., 2017).

A simplified view of the geometry is shown in Figure 9. The

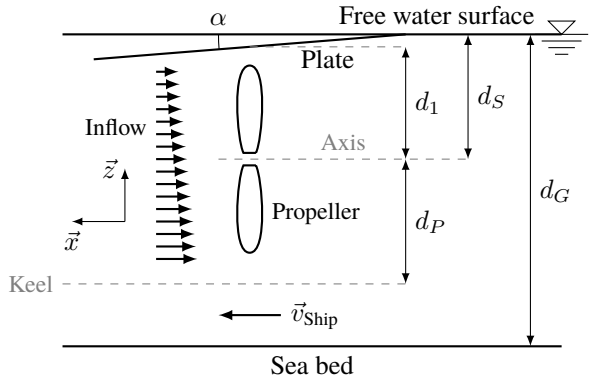

Figure 9: Propeller and hull geometry.

relevant part of the hull above the propeller is simulated by a flat plate. The propeller is the same as in Section 3.2 and is placed below the center of the plate. To simulate the ship wake, a nominal wake field of the ship is extracted from a RANS calculation and placed upstream of the propeller acting as inhomogeneous inflow.

In order to take into account reflection phenomena, a free water surface and a sea bed were added. The positions of the reflection planes correspond to the positions in the full scale measurement.

The discretised geometry is shown in Figure 10. The plate

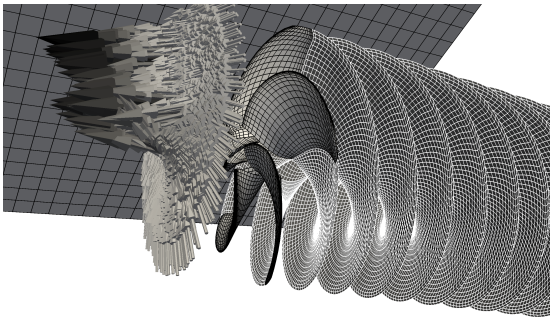

Figure 10: Discretised propeller and hull geometry.

is modelled by 30 panels in longitudinal and 29 panels in transverse direction. The propeller and wake discretisations are similar to those in Section 3.2. The ship wake is modelled by 48616 points (not all shown in Figure 10, the arrows indicates the difference to the undisturbed inflow velocity).

The fluid simulations are carried out with and without cavitation. The sound emission is calculated for each case. The simulation parameters are listed in Table 3.

Table 3: Propeller and hull calculation parameters.

Characteristics			**Value**
Propeller			
Thrust loading condition	c_{Th}		1.232
Geometry			
Propeller axis relative to free surface	d_S	[m]	7.43
Propeller axis relative to plate	d_1	[m]	10.44
Water depth	d_G	[m]	60.0
Angle of plate	α	[°]	6.56
FWH			
Fluid density	ρ_0	$[\mathrm{kg\,m^{-3}}]$	1025.0
Air density	ρ_1	$[\mathrm{kg\,m^{-3}}]$	1.293
Sound speed	c	$[\mathrm{m\,s^{-1}}]$	1500.0
Sea bed reflection factor	R_G		1.0

The resulting normalized pressure amplitudes $\hat{p}^*$ of the blade frequency are shown in Figures 11 and 12 for the calculation without cavitation. For the calculation with

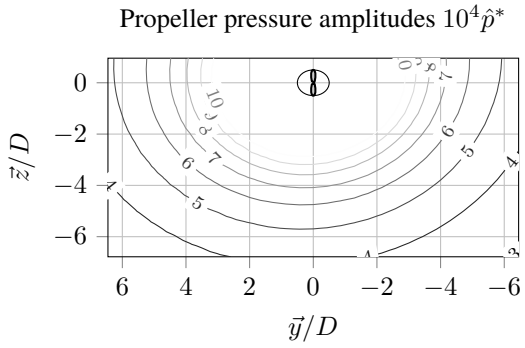

Figure 11: Normalized pressure amplitudes $10^4\hat{p}^*$ (first order) of the non-cavitating propeller and hull without reflections.

cavitation, the normalized pressure amplitudes are shown in Figures 13 and 14. The position and diameter of the propeller is indicated by a small, two-bladed propeller sketch in the diagrams. From the reader's point of view, the rotation direction is clockwise. The hull above the propeller is not shown. The free water surface is placed at the top of the diagrams and the bottom bounding line represents the sea bed. Figure 15 shows the normalized pressure amplitudes $\hat{p}^*$ over the dashed gray lines in Figures 12 and 14. The pressure amplitudes are normalized with Equation (17).

Figure 11 illustrates the concentric sound emission comparable to the cases of the pulsating sphere (see Figure 4) and

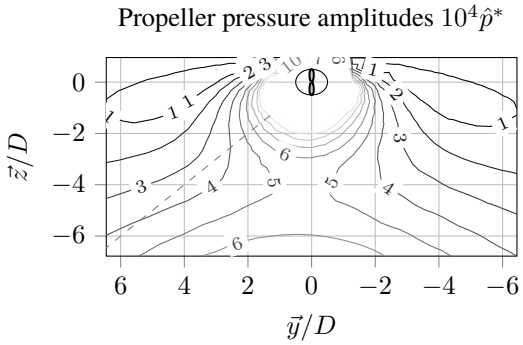

Figure 12: Normalized pressure amplitudes $10^4\hat{p}^*$ (first order) of the non-cavitating propeller and hull with reflections at the free surface and the sea bed.

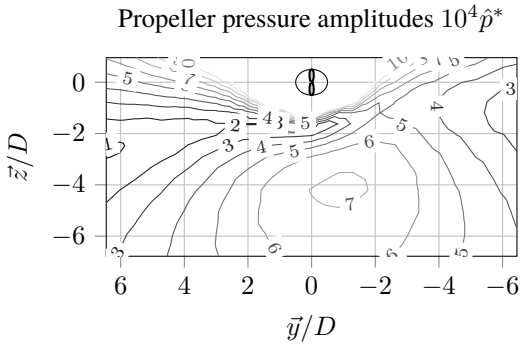

Figure 13: Normalized pressure amplitudes $10^4\hat{p}^*$ (first order) of the cavitating propeller and hull without reflections.

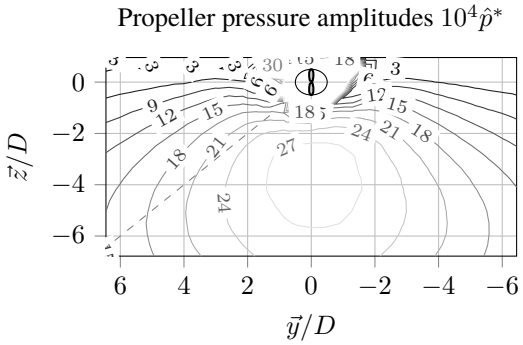

Figure 14: Normalized pressure amplitudes $10^4\hat{p}^*$ (first order) of the cavitating propeller and hull with reflections at the free surface and the sea bed.

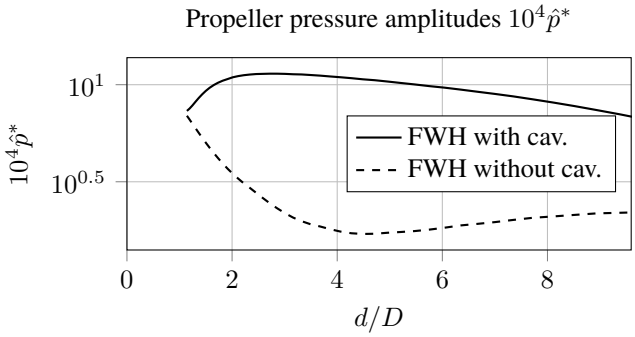

Figure 15: Normalized pressure amplitudes $10^4\hat{p}^*$ (first order) of the non-cavitating and cavitating propeller and hull with reflections at the free surface and the sea bed over line.

the open water test case (see Figure 7). The interaction of the propeller, its rotation direction and the hull results in a not completely symmetric emission. The influence of the reflection planes results in increased amplitudes directly below the propeller and the ship. To the sides and especially near the free water surface the interferences reduce the pressure levels.

In the cavitating case, the amplitudes of the emitted pressure signals from the propeller are increased. This results in a local reflection plane at the hull in the fluid domain. The interference of the FWH pressures from the hull and the propeller results in the pressure amplitudes in Figure 13. The asymmetry of the field is higher compared to the non-cavitating case. The reflections at the free water surface and at the sea bed in Figure 14 result in an increase of the pressure amplitudes. Near the free surface there is a reduction that can also be noticed in the non-cavitating case. Additionally, the asymmetry is reduced compared to Figure 13. The influence of the sea bed reflection shows a similar tendency, as in the non-cavitating case, and so the qualitative pattern of the pressure amplitudes in the lower part of Figure 14 does not change much in comparison with Figure 13.

The comparison to the calculation results with full-scale measurement is given in Figure 16. The measurement point is on the starboard side $120\,\mathrm{m}$ beside the propeller axis in $39\,\mathrm{m}$ depth, outside the contour plots. The sound pressure levels are normalized as follows, according to International Towing Tank Conference (2014, Sec. 2.5.3), to a distance of $d_{\mathrm{ref}} = 1\,\mathrm{m}$:

$$L_S = L_P + 20\log_{10}\left(\frac{d}{d_{\mathrm{ref}}}\right). \tag{18}$$

Measurement results are not available for frequencies below $10\,\mathrm{Hz}$.

In Figure 16a, the calculation results show a large influence of cavitation on the pressure amplitudes, especially when considering the higher-order blade frequencies. The non-cavitating case has large amplitudes only at integer multiples of the blade frequency. The cavitating case shows the same behaviour for the first three blade frequencies. For the higher frequencies, the discrete fluctuation of the cavitation area and thickness dominates the sound emission. This results in a much higher noise level in the cavitating case. Compared to the measurement results, the cavitating case matches fairly well in the second and third blade frequency, but the noise level of the measurement is higher. This should be expected, as not all noise sources are included in the simulation, such as turbulence, structure, rudder, etc. The results show a higher pressure level of the measurement in the thirds plot in Figure 16b. The calculated pressure amplitudes with cavitation match the measurement results at second blade frequency.

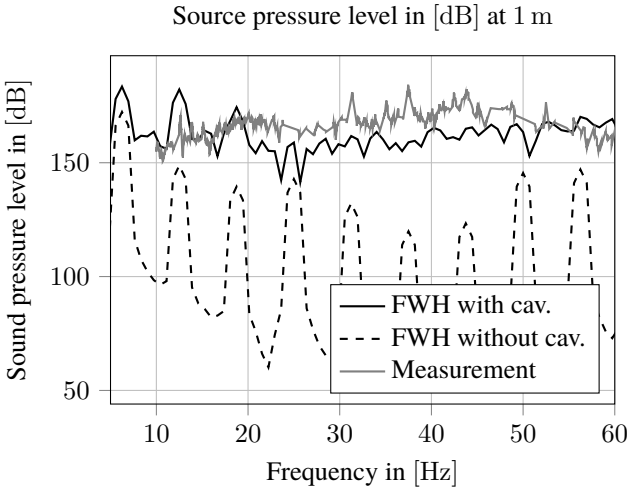

(a) Sound pressure level.

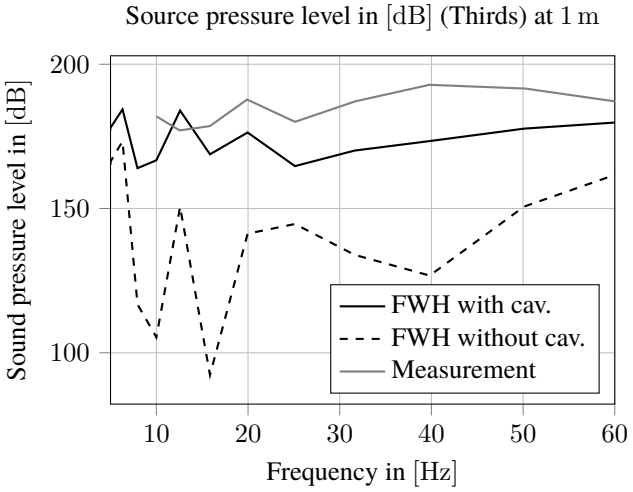

(b) Sound pressure level in thirds.

Figure 16: Sound pressure level of the propeller and hull with reflections at the free surface and the sea bed. Normalized to a distance of 1 m.

4 CONCLUSION

A simulation method for the underwater noise emission prediction for cavitating ship propellers was presented. This is able to consider reflections at the free surface and the sea bed. The results are compared with full-scale measurement data and a good agreement of the calculation and the measurement is achieved. The accuracy of the computation can be increased by modelling the complete ship hull with appendages. Especially the interaction of the propeller slip-stream and the rudder should be taken into account.

5 ACKNOWLEGEMENTS

The full-scale measurement results were kindly provided by Mecklenburger Metallguss GmbH. The first and third author are funded by the BMWi-project (03SX377B) “NoiseLES”. The financial support is highly appreciated.

REFERENCES

Bensow, R. and Liefvendahl, M. . An acoustic analogy and scale-resolving flow simulation methodology for the prediction of propeller radiated noise. In 31th Symposium on Naval Hydrodynamics, Monterey, CA, USA, September 2016.

Berger, S. , Bauer, M. , Druckenbrod, M. , and Abdel-Maksoud, M. . Investigation of Scale Effects on Propeller-Induced Pressure Fluctuations by a Viscous/Inviscid Coupling Approach. Third International Symposium on Marine Propulsors smp’13, 2013. URL http://www.marinepropulsors.com/proceedings/2013/4B.2.pdf.

Brentner, K. S. and Farassat, F. . Modeling aerodynamically generated sound of helicopter rotors. Progress in Aerospace Sciences, 39(2–3):83 – 120, 2003. doi: 10.1016/S0376-0421(02)00068-4.

Farassat, F. and Brentner, K. S. . The Acoustic Analogy and the Prediction of the Noise of Rotating Blades. Theoretical and Computational Fluid Dynamics, 10(1):155–170, 1998. ISSN 1432-2250. doi: 10.1007/s001620050056.

Fine, N. E. . Non-linear Analysis of Cavitating Propellers in Nonuniform Flow. PhD thesis, Massachusetts Institute of Technology, Cambridge, USA, 1992. URL http://hdl.handle.net/1721.1/12564.

Ianniello, S. , Muscari, R. , and Di Mascio, A. . Ship underwater noise assessment by the Acoustic Analogy. part II: hydroacoustic analysis of a ship scaled model. Journal of Marine Science and Technology, 19(1):52–74, 2014a. ISSN 1437-8213. doi: 10.1007/s00773-013-0236-z.

Ianniello, S. , Muscari, R. , and Di Mascio, A. . Ship underwater noise assessment by the acoustic analogy, part III: measurements versus numerical predictions on a full-scale ship. Journal of Marine Science and Technology, 19(2):125–142, 2014b. ISSN 0948-4280. doi: 10.1007/s00773-013-0228-z.

International Towing Tank Conference. Model scale noise measurements. Recommended Procedures and Guidelines 7.5-02-01-05, 2014. URL http://ittc.info/media/4052/75-02-01-05.pdf.

Katz, J. and Plotkin, A. . Low-Speed Aerodynamics. Cambridge University Press, Cambridge, 2 edition, February 2001. ISBN 9780511810329. doi: 10.1017/CBO9780511810329.

Kleinsorge, L. , Klose, R. , Schemmink, S. , and Greitsch, L. . Case Study for the Determination of Propeller Emitted Noise by Experimental and Computational Methods. Fifth International Symposium on Marine Propulsors smp’17, 2017.

Mei, C. C. . Wave propagation, Chapter three, Two dimensional waves. Internet, 2017-01-05, 2004. URL http://web.mit.edu/1.138j/www/material/chap-3.pdf.

Vaz, G. . Modelling of Sheet Cavitation on Hydrofoils and Marine Propellers using Boundary Element Methods. PhD thesis, IST, UTL, Lisbon, Portugal, 2005.

DISCUSSION

Question from Youyiang Wang

Could any information about the calculation time be given?

Author's closure

All calculations are carried out on a twelve core workstation with Intel® Xeon® CPUs, each with $2.6\,\mathrm{GHz}$. The calculation time for the flow simulation of the propeller and hull with cavitation (compare section 3.2) took 58:09:08 hours overall CPU-time for 601 time steps, which leads to an average of 5:48 minutes overall CPU-time per time step. Without cavitation, the overall CPU-time was 22:49:01 hours for 601 time steps, which leads to an average of 2:16 minutes per time step. The sound pressure calculation for the cavitating case took 42:26 minutes overall CPU-time for 361 time steps (the first iterations are skipped), which is similar to the time for the non-cavitating case. Because the calculations are performed with twelve threads, the wall time is approximately $1/8$ of the overall CPU-time for the flow calculation and $1/4$ for the sound pressure calculation.

Question from Serkan Turkmen

How did you define boundary conditions for seabed and free surface in the numerical model?

Author's closure

All flow calculations are performed without considering boundary conditions for the free surface and the sea bed. For the propeller with hull (compare section 3.3), the influence of a symmetry boundary condition at the free surface was investigated, but the influence is negligible and increases the calculation time. The sea bed is assumed as far away from the body, so there is no boundary condition required. In the sound prediction, a reflection model is applied for both boundaries (compare section 2.2.3).

Question from Ronnie Leung

Plots of noise level are only shown for frequencies up to $60\,\mathrm{Hz}$. The frequency seems to be to low to be cavitation noise.

Author's closure

The cavitation model considers only the sheet cavitation pattern on the propeller blades. Single cavitation bubbles are not taken into account. So the predicted noise from the cavitation is the result of the change of the cavitation sheet pattern, which takes place with lower frequencies.

Question from Thomas Lloyd

Have you investigated the influence of the retarded time on the pressure prediction by the FW-H acoustic analogy? This is often neglected in hydro acoustics, assuming acoustic compactness.

Author's closure

For the direct sound path, the retarded time can be neglected for this compact sound sources arrangement. When the reflection is considered, the retarded time is required for a reasonable interference pattern.

Question from Francesco Salvatore

Thank you for this interesting survey. In this kind of model, the cavitation-induced thickness noise is very sensitive to the accuracy of the evolution in time of the cavity pattern. I would like to know the value of the time step was used in calculations and if a sensitivity analysis on the time step has been performed.

Author's closure

A sensitivity analysis was carried out regarding the influence of the time step on the stability of the cavitation pattern. The selected time step duration varied in the range from $1\,^\circ$ to $8\,^\circ$ per time step. In the calculations, a time step magnitude of $3\,^\circ$ per time step was chosen, which leads to a time step magnitude of $0.00\bar{6}\,\mathrm{s}$ (as given in table 2). As the sound prediction is based on the flow calculation, there was no second sensitivity analysis performed.